Research on Engineering Structures & Materials
www.jresm.org

Research Article

Assessment of the harmfulness of corrosion defects in a pressurized pipeline with a single corrosion defect using FEA and ANN

Yassine El Kiri [a], Laidi Zahiri [b], Khalifa Mansouri [c], Zakaria Mighouar [d]

Laboratory of Modelling and Simulation of Intelligent Industrial Systems (M2S2I), ENSET, Hassan II University of Casablanca, Morocco

Article Info

Article History:

Received 26 Oct 2024

Accepted 06 Feb 2025

Keywords:

Pipeline;
Defect;
Corrosion;
Burst pressure;
Finite element method;
Artificial neural network

Abstract

External corrosion is a significant issue that can lead to ruptures in long-distance liquid transportation facilities such as pipelines. Highlighting the need for regular monitoring of their condition, which can compromise their integrity and safety. Three types of external corrosion defects were studied since it is necessary in some to prioritize interventions when multiple defects appear simultaneously on different sections considering burst pressure of the structure. These pressures were determined using numerical simulations in SolidWorks, based on models validated by previous experimental results. An artificial neural network was developed to quickly predict burst pressures, optimizing the network's topology through detailed analysis and thus avoiding the need for complex finite element analyses in the future. The results indicate that the defect having parabolic shape is generally the most detrimental to the structure, although the circumferential defect may be more damaging in certain cases. Additionally, the depth of the defect is a crucial parameter compared to geometric characteristics, emphasizing the importance of continuous monitoring to prevent corrosion risks.

1. Introduction

The transportation of liquid and gaseous hydrocarbons has now become crucial due to the increase in volumes of products used and consumed, emphasizing the need to use large-scale and economically viable means of transportation, notably pipelines [1]. In this context, the installation of pipeline networks has evolved to offer great flexibility in transportation and adaptation to the requirements of the transported products [2]. Pipelines represent the primary means of transportation for oil, gas, water, and various petroleum products [3]. However, their aging, impacts with foreign bodies, as well as exposure to a corrosive environment, can lead to the occurrence of various defects such as cracks, dents, notches, and corrosion [4-8].

According to systematic statistics from the European Gas Pipeline Incident Data Group (EGIG) on incident frequencies concerning gas pipelines, it is evident that incidents related to corrosion and external interferences in these infrastructures represent significant portions to be considered, as shown in Fig. 1 [9]. This highlights the importance of conducting scientific research to counter leaks or explosions resulting from these anomalies.

Corrosion results from the aggressiveness of the soil, environment, and transported products. Over time, it can lead to an increase in roughness, thereby causing a decrease in thickness and mechanical strength of pipelines [10]. Therefore, monitoring and tracking the condition of

*Corresponding author: yassine.elkiri-etu@etu.univh2c.ma
[a]orcid.org/ 0000-0002-8089-8273; [b]orcid.org/ 0000-0003-2685-6088; [c]orcid.org/ 0000-0003-2242-0973; [d]orcid.org/ 0000-0002-0716-8231
DOI: http://dx.doi.org/10.17515/resm2025-502ml1026rs

pipelines remain essential operations for planning maintenance interventions to avoid unexpected fluid transport shutdowns due to leaks or explosions [11-13]. Corrosion of mechanical components in operation poses a significant obstacle in design, as its impacts are observed at various stages, ranging from mining extraction to the design, manufacturing, usage, reuse, and recycling phases [14]. When a component undergoes corrosion, whether it experiences generalized or localized corrosion, it undergoes geometric modifications and alters its surface condition, as shown in Fig. 2. Furthermore, the formation of localized corrosion zones creates areas of high stress concentration, thereby becoming preferential sites for crack initiation and propagation [15].

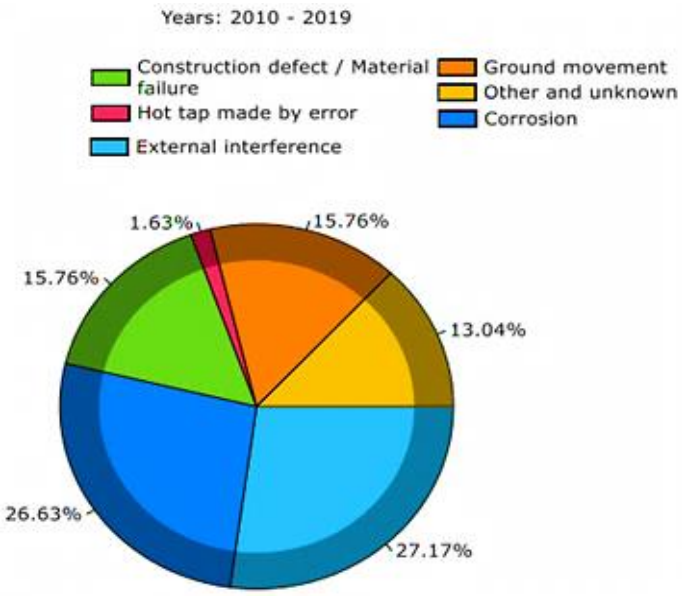

Fig. 1. Distribution of gas pipeline incidents (2010-2019), 11th EGIG-report [9]

Corrosion results from the aggressiveness of the soil, environment, and transported products. Over time, it can lead to an increase in roughness, thereby causing a decrease in thickness and mechanical strength of pipelines [10]. Therefore, monitoring and tracking the condition of pipelines remain essential operations for planning maintenance interventions to avoid unexpected fluid transport shutdowns due to leaks or explosions [11-13]. Corrosion of mechanical components in operation poses a significant obstacle in design, as its impacts are observed at various stages, ranging from mining extraction to the design, manufacturing, usage, reuse, and recycling phases [14]. When a component undergoes corrosion, whether it experiences generalized or localized corrosion, it undergoes geometric modifications and alters its surface condition, as shown in Fig. 2. Furthermore, the formation of localized corrosion zones creates areas of high stress concentration, thereby becoming preferential sites for crack initiation and propagation [15].

Fig. 2. An excavated gas pipeline subject to external corrosion [16]

In the oil and gas industry, numerous assessment standards are utilized to evaluate the residual strength of corroded pipelines. Among these, standards such as ASME B31G [17], Modified B31G [18], RSTRENG [19], PCORRC [20] and DNV RP-F101 [21]. are widely practiced for pipeline

inspection and maintenance, ensuring their proper functioning. However, most of these standards focus solely on assessing corroded pipelines [22].

Some studies have utilized finite element analysis (FEA) results to develop analytical solutions that can be implemented as quickly as standards and codes while preserving the accuracy of the finite element method [23-25]. Studies [23] have analyzed the residual strength of a pipeline exhibiting a circumferential corrosion groove under internal pressure, employing seven equations that incorporate the length and depth of the defect. The results obtained demonstrated satisfactory agreement with finite element analyses (FEA), exhibiting errors below 5%. It is noteworthy that the corrosion defect modeled in references [22, 23] was idealized as rectangular, this configuration being frequently adopted for assessing the corrosion-induced rupture of pipelines [21, 26].

Commonly employed standards for assessing the burst pressure of corroded pipelines exhibit limitations, particularly when dealing with complex and non-idealized loading configurations. These limitations result in conservative estimates, frequently being oversized. To address these inadequacies, recent studies have explored the application of artificial intelligence (AI) techniques, specifically through the development of an artificial neural network (ANN) model. This model, trained on a synthetic dataset generated using the finite element method (FEM), aims to accurately reproduce FEM results while overcoming the restrictions of traditional standards and avoiding the need for volumetric FEM analyses [22,27].

Several research works have successfully developed neural networks capable of predicting the burst pressure of a corroded pipeline based on finite element analysis (FEA) results [28-31]. This advancement encourages us to also apply artificial neural networks (ANN) in evaluating the harmfulness of three types of corrosion defects.

Despite research conducted on pipeline defects, a gap is observed in the evaluation of the harmfulness of certain defects present in pipelines, notably the most damaging corrosion form depending on the applied external load. To address this gap, our study specifically focuses on evaluating the degree of harmfulness of the three common forms of corrosion: rectangular, parabolic, and circumferential, using the results of the artificial neural network (ANN).

The analysis will enable a classification of the severity of the three considered types of corrosion defects, through the application of standardized formulations within the field. The evaluation will be based on the ASME B31G code [17] for parabolic-shaped defects [18], the DNV-RP-F101 code [21] for rectangular-shaped defects, and equations derived from prior research [23] for circumferential-shaped defects. A comparison of the results obtained using the neural network approach for these three types of corrosion defects will be conducted. An overview of some research works on corrosion defects in pressurized pipelines, using FEA and ANN to evaluate burst pressure, as shown in Table 1.

Table 1. Recent prior research on pressurized pipelines affected by corrosion

References	Type of defect	Loading	Methods
Michael Lo et al.[22] (2022)	Rectangular	Internal pressure with axial compressive stress	FEA/ANN
Arumugam et al. [23] (2020)	Circumferential	Internal pressure	FEA
Arumugam et al. [32] (2020)	Rectangular	Internal pressure with axial compressive stress	FEA
Xu et al. [33] (2017)	Rectangular circumferential in interaction	Internal pressure	FEA/ANN
Kumar et al. [34] (2022)	Circumferential interaction	Internal pressure with axial compressive stress	FEA/ANN

These research works illustrate the growing importance of integrating advanced numerical modeling techniques such as FEA and ANN in assessing the safety and reliability of pressurized pipelines. These approaches enhance understanding of the factors influencing pipeline strength and enable more informed decisions regarding maintenance and operation.

2. Materials and Methods

This article proposes a two-step approach to assess the stability of corroded and pressurized pipelines. In the first step, the finite element method (FEA) is used to validate three numerical models representing different types of external corrosion on the pipeline. The aim of this step is to establish numerical models of these corroded pipelines to predict the internal pressure required to avoid bursting near the defect zones. This prediction is based on stress field analysis according to the Von Mises criterion, which is commonly used to assess plastic deformation in materials. The length and depth of defects are the key geometric parameters in evaluating burst pressure. To quantify their influence on this pressure, a parametric analysis is conducted by varying these magnitudes, thereby generating a structured database. This dataset, characterized by the diversity of defect geometries and their associated burst pressures, will serve as the foundation for the development of a new predictive numerical equation. This equation will be developed through artificial neural network (ANN) learning, a machine learning technique recognized for its ability to model complex relationships between variables.

Once the burst pressure prediction is made using the artificial neural network, we proceed to evaluate the harmfulness of the three identified defect types. This evaluation aims to analyze the impact of these defects on the normal operation of the pipeline. Furthermore, it aims to deduce the geometric parameter that most rapidly influences burst, which could prioritize inspections and repairs based on this parameter.

In summary, the proposed approach combines numerical analysis techniques, modeling by artificial neural networks, and harmfulness assessment to evaluate the stability of corroded and pressurized pipelines, as well as to identify critical defects requiring particular attention.

2.1 Numerical Model

The assumption that the corrosion defect adopts a rectangular shape was chosen because this approach is widely used for assessing pipeline corrosion and has been validated by several researchers, thus providing fairly accurate predictions of burst pressure [35-39]. To reduce computation time without compromising result accuracy, a reduced-size model was employed in this study [40]. This model consists of a symmetric quarter-pipe, as illustrated in Fig. 3, to faithfully represent the actual geometry of the pipeline. Additionally, the pipe was specified with a length of

2,000 mm to avoid any influence of end conditions on the corrosion defect zones during finite element analysis.

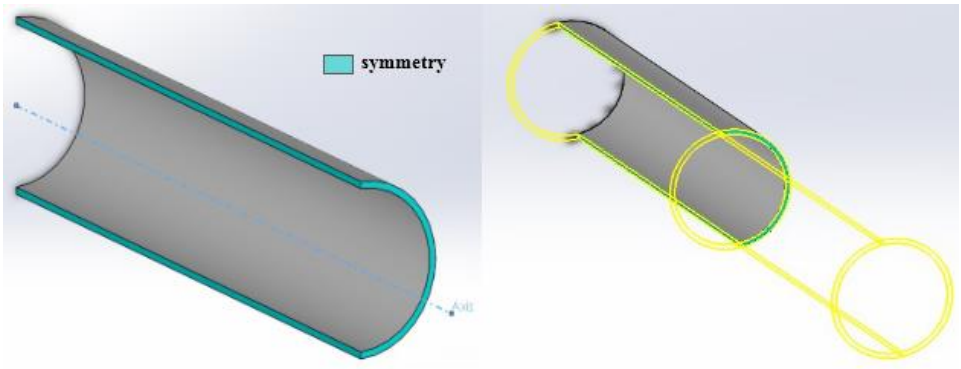

Fig. 3. API 5L X65 quarter-pipe model

The 3D modeling software SolidWorks was used to create the models. Since this study focuses on single corrosion defects (rectangular, parabolic, and circumferential) with symmetric geometries, only a quarter of the pipe was modeled to accurately represent the conduit's real geometry. Furthermore, the pipelines were modeled with a length of 1,000 mm, corresponding to half the length of the model.

2.2 Mechanical and Geometric Properties of the Numerical Model

The numerical model developed in SolidWorks involves digitally modeling a section of a corroded pipeline subjected to internal pressure. We will study the quality of the API 5L X65 steel pipe. The mechanical properties of this grade are presented in Table 2. This numerical module aims to replace analytical expressions that evaluate burst pressure based on the form of corrosion defect. The geometric dimensions for the numerical pipeline model can be found in Table 3.

Table 2. Mechanical properties of steel tube API 5L X65 [41]

Mechanical properties	Values
Modulus of Elasticity, E	210 GPa
Poisson's ratio, ϑ	0,3
Yield Strength, σ_y	464 MPa
Ultimate tensile strength, σ_u	563 MPa
True ultimate tensile strength, σ_{uts}	629 MPa

Table 3. Geometric properties of the pipeline

Geometric properties	Values
Pipe outside diameter, D (mm)	250
Length of pipe, L (mm)	2000
Wall thickness, t (mm)	10

2.3 Model Validation

Finite element (FE) modeling of irregular defects or local instabilities requires a careful and iterative approach. Mesh refinement, appropriate selection of boundary conditions, and validation against experimental data are essential to obtain reliable predictions, particularly for the determination of burst pressure. The validation of the finite element analysis (FEA) model was conducted by comparing simulation results with experimental data obtained by Lo et al. [22]. who performed burst tests on two specimens, designated LD and LF. To evaluate the influence of spatial discretization parameters and boundary conditions, a sensitivity analysis was carried out. This study examined three mesh generation methodologies (standard, curvature-based, and curvature-based with conformal mesh transitions) as well as two boundary condition configurations:

- Case 1: A planar support on one face, combined with a longitudinal edge fixed support.
- Case 2: Only a longitudinal edge fixed support.

The comparative analysis of numerical results for different combinations of mesh and boundary conditions revealed a significant influence of these parameters on burst pressure prediction. The results of this sensitivity study are summarized in Table 4. For both specimens studied, the comparison of burst pressures predicted by FEA and experimental values demonstrated satisfactory agreement, with a relative error of less than 10% for a curvature-based mesh with Case 1 boundary conditions, thus providing a more realistic numerical model.

The validation of the numerical model was supported by a second comparative analysis. The theoretical burst pressure of the intact pipe, calculated using Eq (1) [42], was compared to the FEA-estimated burst pressure of the intact pipe, revealing an error of 2.37% (Table 5). This slight discrepancy can be attributed to several sources of uncertainty, including:

- The idealization of the defect geometry.
- The choices of discretization parameters (finite elements, element size).
- Inherent errors in numerical calculation methods.

These small errors confirm the appropriate choice of mesh parameters and boundary conditions.

$$P_i = \frac{\sigma_{uts}.t}{r_i} \tag{1}$$

Table 4. Failure pressure from burst tests compared with failure pressure predicted in FEA

Specimen	Failure pressure from burst tests [22]	Boundary conditions	Mesh (Mesh generator)	Failure pressure from FEA (MPA)	Relative error (%)
LD	19.80 MPa	Planar support and Fixed support	Standard mesh	32,62	64,74
			Curvature-based mesh	20,78	4,95
			Blanded Curvature-based mesh	24,51	23,78
		Fixed support	Standard mesh	36,12	82,42
			Curvature-based mesh	29,48	48,89
			Blanded Curvature-based mesh	25,35	28,03
LF	15.00 MPa	Planar support and Fixed support	Standard mesh	26,05	73,67
			Curvature-based mesh	15,89	5,94
			Blanded Curvature-based mesh	20,45	36,34
		Fixed support	Standard mesh	29,5	96,67
			Curvature-based mesh	23,17	54,47
			Blanded Curvature-based mesh	21,71	44,74

Table 5. Comparison between theoretical and numerical intact pressure

Theoretical burst pressure	Numerical burst pressure	Relative error
54.7 MPa	56 MPa	2,37 %

2.4 Meshing and Boundary Conditions

2.4.1 Rectangular Defect

Fig. 4 depicts the rectangular defect located at the center of the studied pipe. For symmetry reasons, only a quarter of the defect has been represented. The geometric characteristics of the defect are schematically shown in the same figure. Pressure has been applied to the internal section of the pipe, while two boundary conditions have been imposed: a planar support on the yellow facet and a fixed boundary condition on the bottom red line (Fig. 4). The quality and accuracy of the computational results are highly dependent on the characteristics of the mesh used. Therefore, the essential parameters defining the mesh are clearly presented in Table 6, allowing for a complete understanding of the discretization strategy employed.

Table 6. Mesh parameters

Mesh type	Rectangular defect volume mesh	Parabolic defect volume mesh	Circumferential defect volume mesh
Mesh generator used		Curvature-based mesh	
Jacobian points for high-quality mesh	At the nodes	16 Points	At the nodes
Maximum element size	35,3 mm	25,186 mm	30,056 mm
Minimum element size	35 mm	24,745 mm	17,68 mm
Mesh quality		Draft	
Total number of nodes	788	1818	1035
Total number of elements	2123	5165	2824
Maximum aspect ratio	10,245	4,911	18,236
% of elements with aspect ratio < 3	36,3	95,4	60,1
% of elements with aspect ratio > 10	0,094	0	0,46

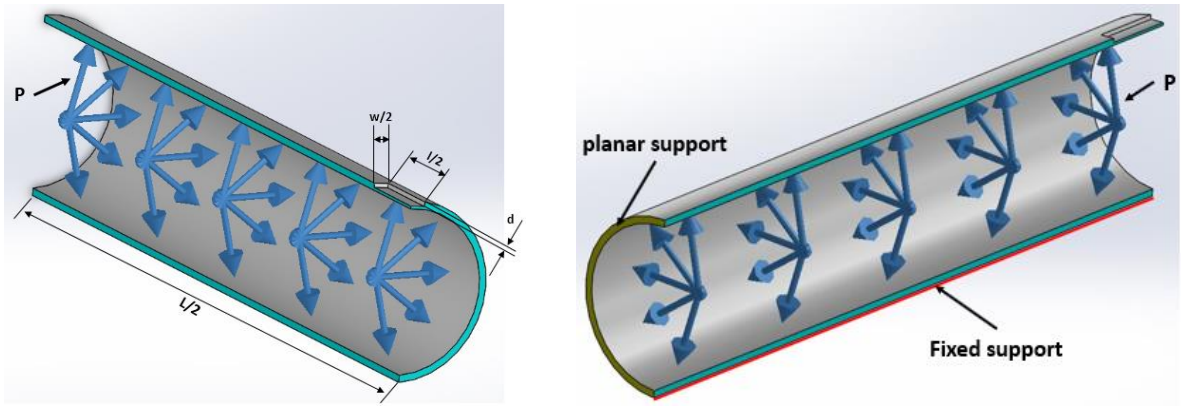

(a) (b)

Fig. 4. (a) Geometric characteristics of the rectangular defect, (b)boundary conditions and loading

2.4.2 Parabolic Defect

Fig. 5 illustrates the parabolic defect localized at the center of the examined pipeline. Given the symmetry of the pipe, only a quarter section of the defect is represented. The geometric characteristics of the defect are schematically shown in the same figure.

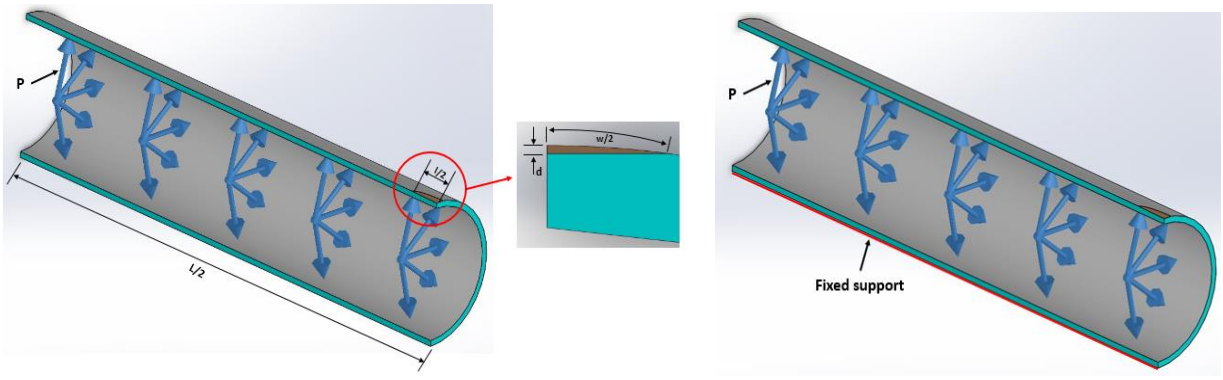

(a) (b)

Fig. 5. Geometric characteristics of the parabolic defect (a), boundary conditions and loading (b)

Pressure has been applied to the internal section of the pipe, while a fixed boundary condition is imposed on the bottom red line, as shown in Fig. 5. The mesh parameters are represented in Table 6.

2.4.3 Circumferential Defect

Fig. 6 depicts a circumferential defect localized at the center of the examined pipeline. Due to the pipe's symmetry, only a quarter section representing the defect is visible. The geometric characteristics of this defect are schematically shown in the same figure. Pressure has been applied to the internal section of the pipe. Two boundary conditions have been defined: a planar support on the yellow facet and a fixed boundary condition on the bottom red line, as shown in Fig. 6. The mesh parameters are represented in Table 6.

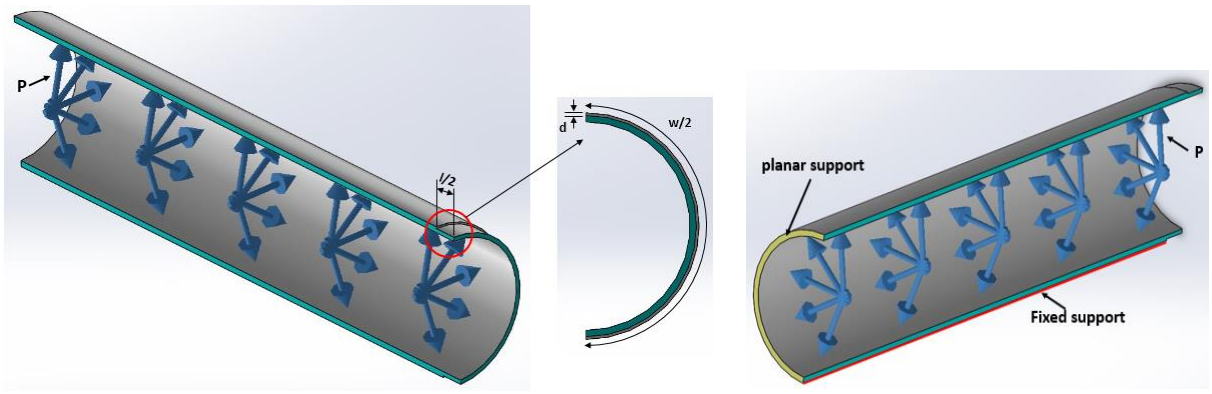

(a) (b)

Fig. 6. (a) Geometric characteristics of the circumferential defect, (b) boundary conditions and loading

2.5 Geometric Parameters of the Study

In this study, we examined the length and depth of a corrosion defect as key variables in determining the burst pressure of a pipeline. These parameters are specified in Table 7, with the defect length ranging from 40 to 220 mm in increments of 20 mm, and the depth ranging from 1 to 6 mm in increments of 1 mm. Fig. 7 and 8 illustrate the shapes of three types of defects.

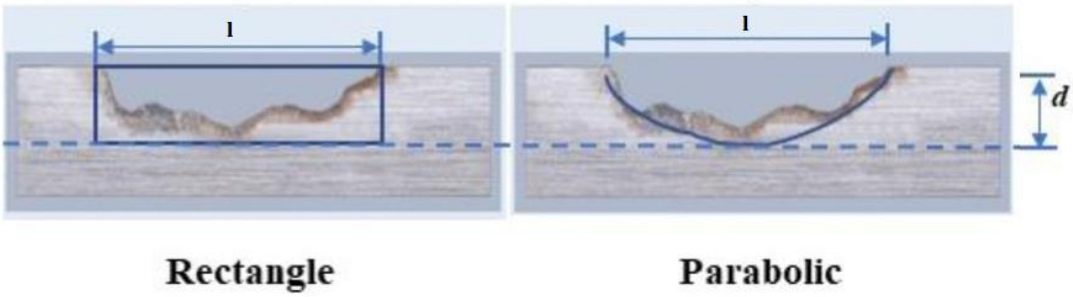

Fig. 7. Geometric dimension of a rectangular and parabolic corrosion defect on pipes [43]

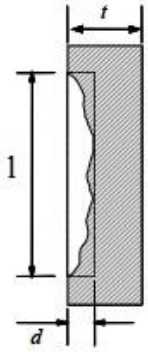

Fig. 8. Geometric dimension of a circumferential corrosion defect [44]

The defect width, denoted as "w," was not considered in this analysis as its impact on the rupture resistance of a corroded pipeline subjected to internal pressure is deemed negligible [17,21,32,23]. Using the parameters listed in Table 7, the burst pressures obtained via the Finite Element Method (FEM) were used to create a training dataset for the Artificial Neural Network (ANN). The geometric dimensions required for the FEA parametric study are detailed in Table 7.

Table 7. Geometric defect parameters

Defect depth, d (mm)		1-2-3-4-5-6
Defect length, l (mm)		40-60-80-100-120-140-160-180-200-220
Defect width, w (mm)	- rectangular defect	20°
	- parabolic defect	20°
	- circumferential defect	$\pi.250$

2.6 Burst Condition

Various criteria have been proposed in previous studies to predict the burst pressure of pipelines with corrosion defects [45]. However, the Finite Element Analysis (FEA) method in SolidWorks cannot anticipate local instability, such as necking, which often leads to final burst. Therefore, accurately predicting the burst pressure of a corroded pipeline using FEA is challenging unless an appropriate rupture criterion is well defined during the simulation, as highlighted by several previous studies [46]. When the effective von Mises stress reaches σ_{uts} throughout the wall, the corresponding internal pressure can be defined as the burst pressure. Predicting burst pressure based on σ_{uts} provides more accurate results, as the failure mechanism is controlled by plastic collapse, notably due to the high toughness of the material under study [47].

In this article, the rupture criterion for the corroded pipeline is based on the local stress in the defect area. Burst occurs when the local stress in this area exceeds the ultimate tensile strength. We applied the Von Mises theory in SolidWorks to analyze stress distribution in the corroded pipe. Cylindrical coordinates are used in the numerical model to detail the three stress components present in the pipe, namely: axial, radial, and circumferential stress, which define the effective Von Mises stress in cylindrical coordinates [48], as shown in Eq (2).

$$\sigma_e = \sqrt{\frac{1}{2}[(\sigma_h - \sigma_r)^2 + (\sigma_h - \sigma_l)^2 + (\sigma_r - \sigma_l)^2]} \tag{2}$$

2.7 Burst Pressure Using the Theoretical Approach, $P_{f,ana}$

This paper presents a study of three common methods for evaluating the burst pressure of pressurized pipelines: the DNV code for longitudinal rectangular defects, ASME B31G for parabolic defects, and the equations from reference [23] for circumferential defects. Both ASME B31G and the equations from [23] incorporate defect geometry into their calculations.

- DNV-RP-F101 code [21]

$$P_{f,ana} = \frac{2.t.\sigma_y.(1-\frac{d}{t})}{(D-t).(1-\frac{d}{t.Q})} \quad \text{With} \quad Q = \sqrt{1+0.31.(\frac{l}{\sqrt{D.t}})^2} \tag{3}$$

- ASME B31G code [17]

$$P_{f,ana} = \frac{2.1,1.\sigma_y.t}{D}.\frac{(1-0,66.(d/t)}{(1-\frac{0,66(\frac{d}{t})}{M_F})} \quad \text{if} \quad \sqrt{0.8.\left(\frac{D}{t}\right).(\frac{l}{D})^2} \leq 4 \tag{4}$$

With $M_F = \sqrt{1+0,8.\left(\frac{l}{D}\right)^2.(\frac{D}{t})}$

- Equations developed by Arumugam et al. [23]

$$P_{f,ana} = P_i.\left(1 - 3{,}738.\left(\frac{d}{t}\right)^{1{,}785}.\left(\frac{l}{D}\right)^{1{,}094}\right) \quad \text{if} \quad \frac{d}{t} \le 0{,}4 \text{ and } \frac{l}{D} \le 0{,}4 \tag{5}$$

$$P_{f,ana} = P_i.\left(1 - 1{,}362.\left(\frac{d}{t}\right)^{1{,}431}.\left(\frac{l}{D}\right)^{0{,}333}\right) \quad \text{if} \quad \frac{d}{t} \le 0{,}4 \text{ and } 0{,}4 < \frac{l}{D} \le 0{,}8 \tag{6}$$

$$P_{f,ana} = P_i.\left(1 - 1{,}127.\left(\frac{d}{t}\right)^{1{,}280}.\left(\frac{l}{D}\right)^{0{,}176}\right) \quad \text{if} \quad \frac{d}{t} \le 0{,}4 \text{ and } 0{,}8 < \frac{l}{D} \le 1{,}2 \tag{7}$$

$$P_{f,ana} = P_i.\left(1 - 1{,}714.\left(\frac{d}{t}\right)^{1{,}627}.\left(\frac{l}{D}\right)^{0{,}536}\right) \quad \text{if} \quad 0{,}4 < \frac{d}{t} \le 0{,}8 \text{ and } 0{,}1 < \frac{l}{D} \le 0{,}4 \tag{8}$$

$$P_{f,ana} = P_i.\left(1 - 1{,}058.\left(\frac{d}{t}\right)^{1{,}248}.\left(\frac{l}{D}\right)^{0{,}120}\right) \quad \text{if} \quad 0{,}4 < \frac{d}{t} \le 0{,}8 \text{ and } 0{,}4 < \frac{l}{D} \le 0{,}8 \tag{9}$$

$$P_{f,ana} = P_i.\left(1 - 0{,}999.\left(\frac{d}{t}\right)^{1{,}129}.\left(\frac{l}{D}\right)^{0{,}039}\right) \quad \text{if} \quad 0{,}4 < \frac{d}{t} \le 0{,}8 \text{ and } 0{,}8 < \frac{l}{D} \le 1{,}2 \tag{10}$$

2.7 Comparative Analysis of Theoretical and Numerical Burst Pressures

The determination of burst pressure is conditioned by the defect geometry. We progressively modified this geometry by adjusting the defect length (denoted as "l") and depth (denoted as "d"), while maintaining its width at a value of 20° for the rectangular and parabolic defects and π.D for the circumferential defect. These adjustments were made to closely approximate the actual geometry of corrosion defects. The burst pressures calculated by the DNV method, the ASME B31G code, and the equations of Arumugam et al. were normalized with respect to the intact pressure. The theoretical pressures in Fig. 9 were determined by varying the geometric parameters of the defects, as illustrated in Table 8. For each type of defect, we studied 60 specimens obtained by combining six variations of the d/t ratio with ten variations of the l/D ratio.

Table 8. Geometric parameters of the three types of defects

$\boldsymbol{l/D}$	0,16-0,24-0,32-0,4-0,48-0,56-0,64-0,72-0,8-0,88
$\boldsymbol{l/\sqrt{Dt}}$	0,8-1,2-1,6-2-2,4-2,8-3,2-3,6-4-4,4
$\boldsymbol{d/t}$	0,1-0,2-0,3-0,4-0,5-0,6

The analysis of the numerical models in SolidWorks demonstrated a satisfactory correlation with the three methods deployed, as evidenced by the relative error values ranging from -6.24% to 8.29% for the circumferential defect, -5.42% to 7.75% for the parabolic defect, and -9.95% to 7.45% for the rectangular defect, as shown in Fig. 10. These error margins, all below 10%, indicate that this numerical approach is capable of predicting the burst pressure of a corroded pipe with geometric parameters within the studied range, thereby validating our numerical model.

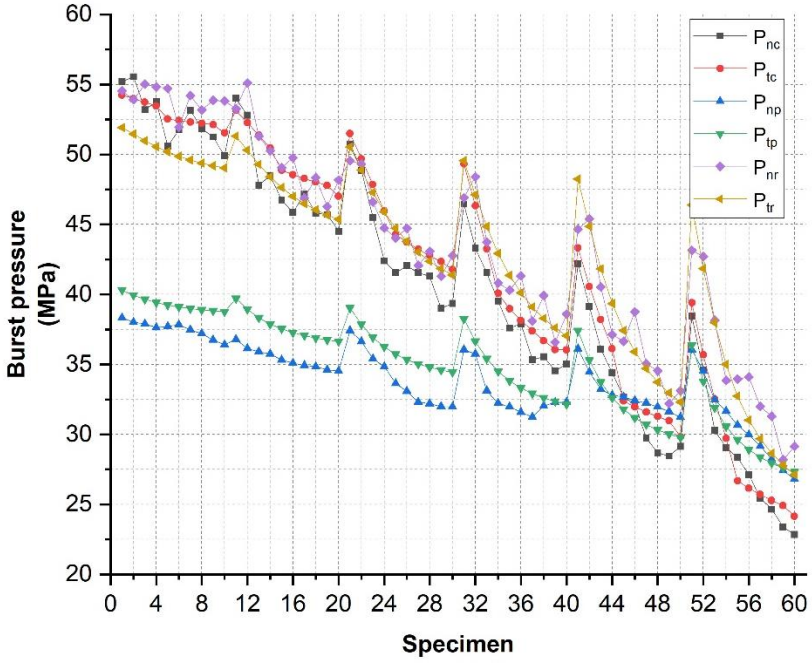

Fig. 9. Evolution of theoretical and numerical burst pressure

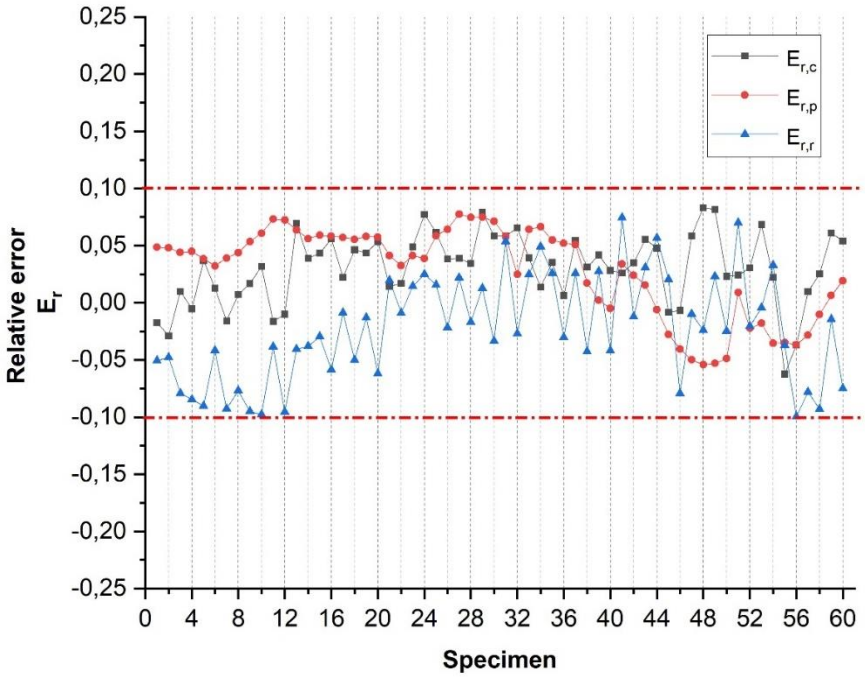

Fig. 10. Relative error between theoretical and numerical pressure of the three defects

2.8 Burst Pressure Prediction Using an Artificial Neural Network

2.8.1. Flowchart for Determining the Optimal Neural Network Topology

Using artificial intelligence in scientific domains has become an alternative approach to numerical simulation, facilitating the prediction of outcomes for complex problems through mathematical equations based on the principle of machine learning from pre-established results (dataset). The structure of the artificial neural network will be developed using Matlab R19a software, with a dataset distributed as follows: 70%, 80%, and 90% for training, and 30%, 20%, and 10% for testing. This data comes from a model validated through numerical simulation in SolidWorks software.

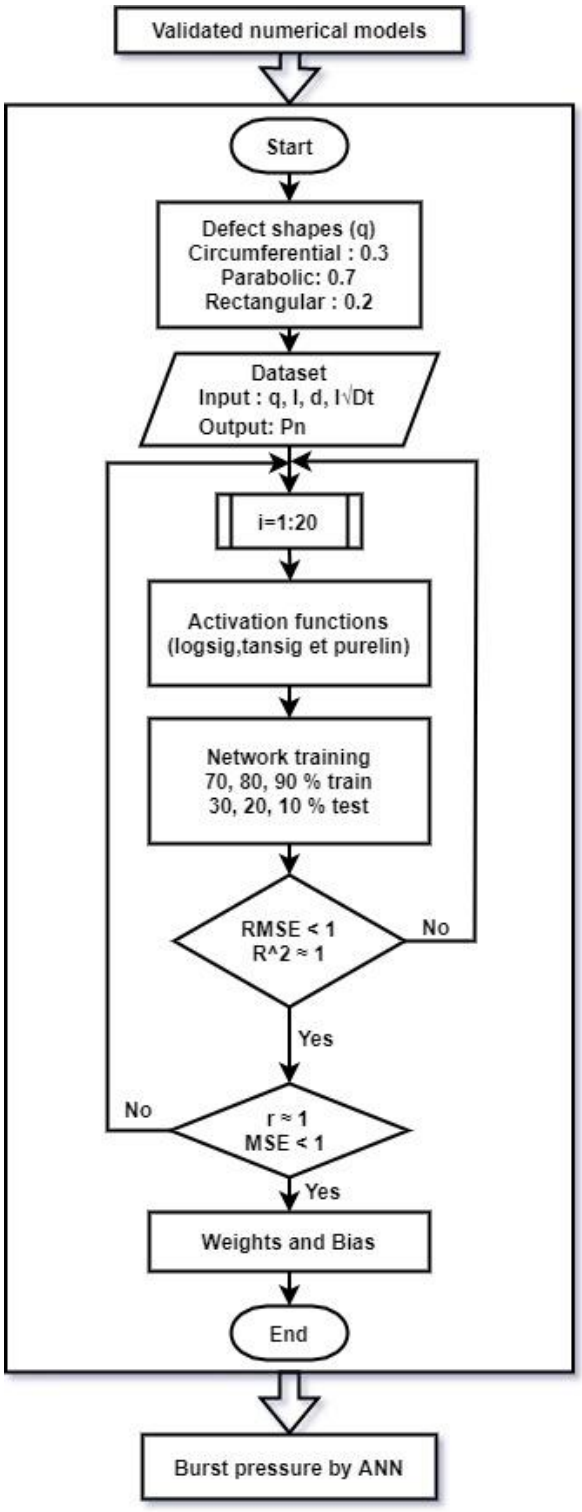

Fig. 11. Flowchart of the steps for optimal neural network selection

We will select a neural network with a single hidden layer, evaluated based on two metrics: a root mean square error (RMSE) below 1 and a coefficient of determination (R^2) close to 1. A loop testing 1 to 20 neurons in the hidden layer was carried out to determine the optimal number of neurons needed to achieve the desired accuracy. Various configurations of the three most commonly used activation functions in machine learning (tansig, logsig, and purelin) were tested, along with different dataset splits between training and testing.

Using Matlab R19a, the structure will be validated according to two complementary metrics: a correlation coefficient (r) close to 1 and a mean square error (MSE) below 1 (Fig.11). The weights

and biases obtained from the selected neural network enable highly accurate prediction of the burst pressure of a pressurized pipeline with a circumferential, parabolic, or rectangular corrosion defect.

2.8.2 Burst Pressure Prediction

Through the use of artificial neural networks, we developed a structure in Matlab R19a to predict the burst pressure of a pressurized pipeline with rectangular, parabolic, and circumferential corrosion defects. The objective was to develop a single hidden layer neural network capable of providing highly accurate results. To achieve this, we explored various configurations, varying the number of neurons in the hidden layer from 1 to 20 using a for loop (for i=1:20), as well as different activation functions (purelin, logsig and tansig) [50], These functions are most suitable in the linear regression problem [22, 33, 34]. Random weights were assigned to the network input for each type of defect, denoted as q, namely: 0.3 for circumferential, 0.7 for parabolic, and 0.2 for rectangular. The network was trained using gradient backpropagation, adjusting the weights and biases of each neuron to minimize the error between the predictions and the actual data [49]. Given the relatively small size of the numerical dataset, with approximately 180 samples, an analysis of the effect of data distribution on prediction accuracy was conducted. The dataset was divided into two portions according to three different ratios: 70%, 80%, and 90% for training, and 30%, 20%, and 10% for testing. To ensure prediction accuracy, we opted for 1000 training epochs, with a maximum of 500 validation failures to refine the learning phase. At each iteration, a combination of activation functions among purelin, logsig, and tansig was selected. At the end of execution, we evaluated the model's performance using four metrics: root mean square error (RMSE) Eq (11), mean squared error (MSE) Eq (12) [51], coefficient of determination (R^2) Eq (13) and correlation coefficient (r) Eq (14) [52].

- Expression of activation functions [50]

Sigmoid	Hyperbolic tangent	Lineair
$\boldsymbol{f(n) = \frac{1}{1 + e^{-n}}}$	$f(n) = \frac{2}{1 + e^{-2n}} - 1$	$f(n) = n$

- Expression of root mean squared error (RMSE) and mean squared error (MSE) [51]

$$RMSE = \sqrt{\frac{1}{m}\sum_{i=1}^{m}(y_i - \hat{y}_i)^2} \tag{11}$$

$$MSE = \frac{1}{m}\sum_{i=1}^{m}(y_i - \hat{y}_i)^2 \tag{12}$$

- Expression of coefficient of determination (R^2 or R-squared) and correlation coefficient (r) [52]

$$R^2 = 1 - \frac{\sum_{i=1}^{m}(y_i - \hat{y}_i)^2}{\sum_{i=1}^{m}(y_i - \bar{y})^2} \tag{13}$$

$$r = \frac{\sum_{i=1}^{m}(y_i - \bar{y}) * \left(\hat{y}_i - {\sum_{i=1}^{m}\hat{y}_i}/{m}\right)}{\sqrt{\sum_{i=1}^{m}(y_i - \bar{y})^2 . (\hat{y}_i - {\sum_{i=1}^{m}\hat{y}_i}/{m})^2}} \tag{14}$$

Fig. 12, 13, and 14 present the R^2 and RMSE metrics for various configurations of activation functions between the hidden layer and the output layer, as well as the data ratio for the training and testing phases, covering the 20 models examined to assess the relevance of the chosen model. In Fig. 12, the exploration begins with the use of the purelin activation function for the hidden layer

and three activation function options for the output layer. The analysis of this figure reveals an inability to achieve the desired accuracy in all three cases, indicated by a coefficient of determination far from 1 and significant fluctuations in RMSE between the training and test sets.

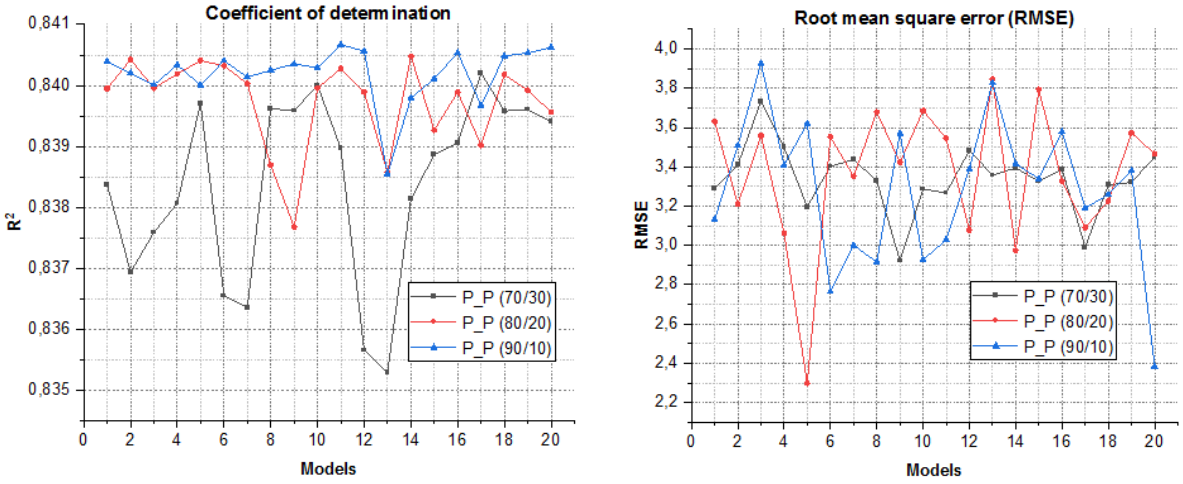

(a)

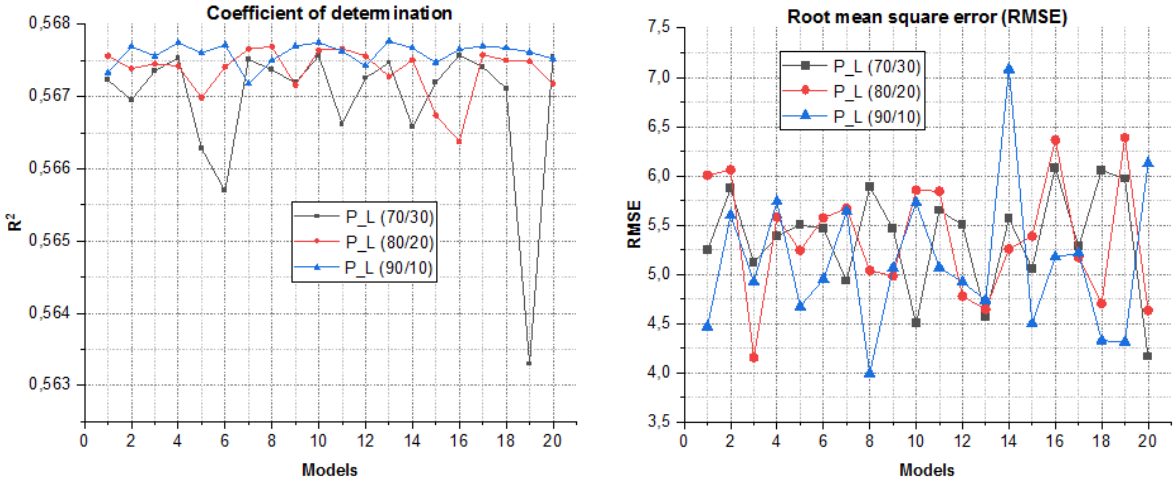

(b)

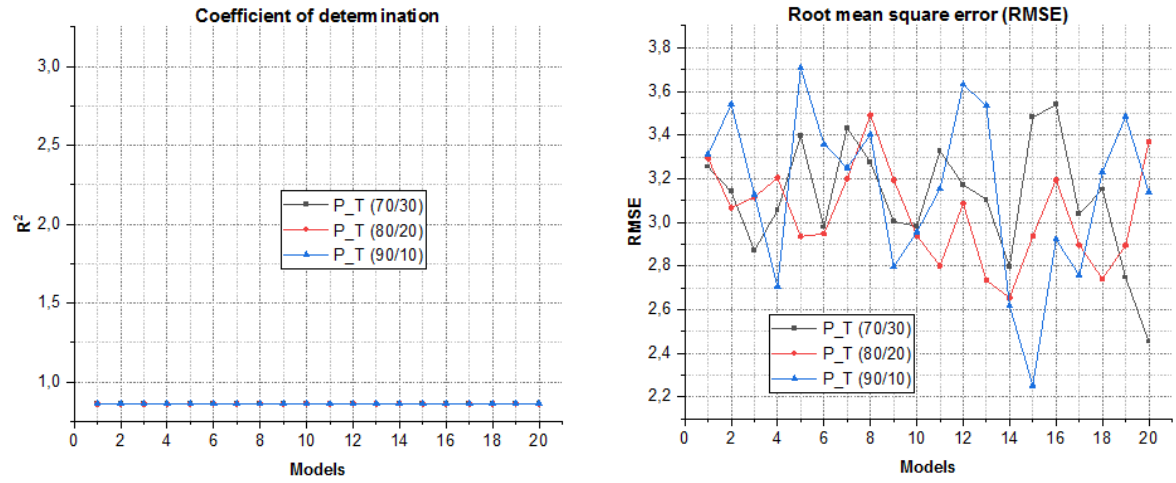

(c)

Fig. 12. Performance of 20 models evaluated by R^2 and RMSE metrics as a function of activation; (a) purelin-purelin, (b) purelin-logsig and (c) purelin-tansig

In contrast, in Fig. 13, an improvement is observed, where the RMSE values for training and testing become closer and decrease in cases a and c, suggesting an enhancement in learning. Additionally, a gradual improvement in the coefficient of determination is noted, particularly in case c with the use of the tansig function in the output layer.

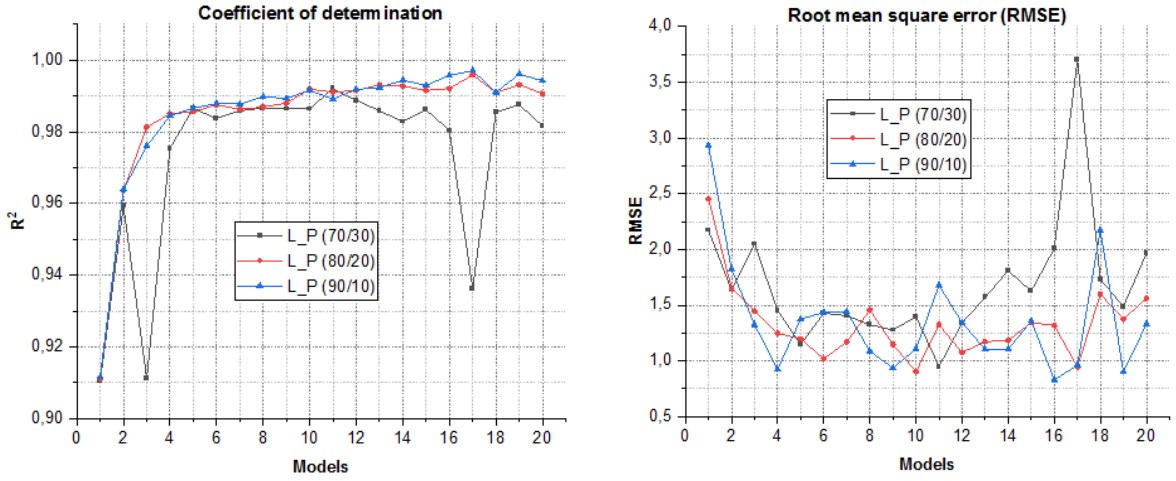

(a)

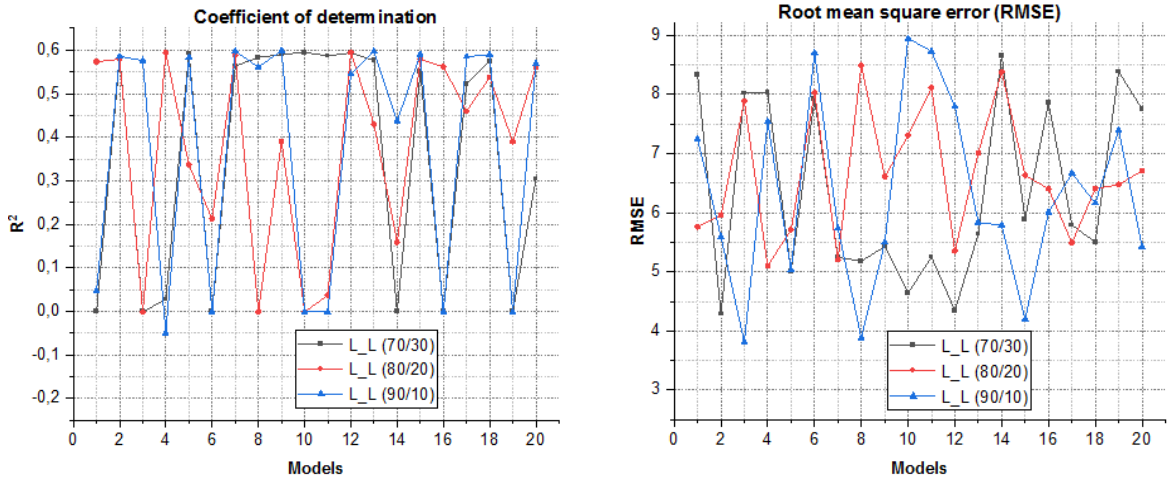

(b)

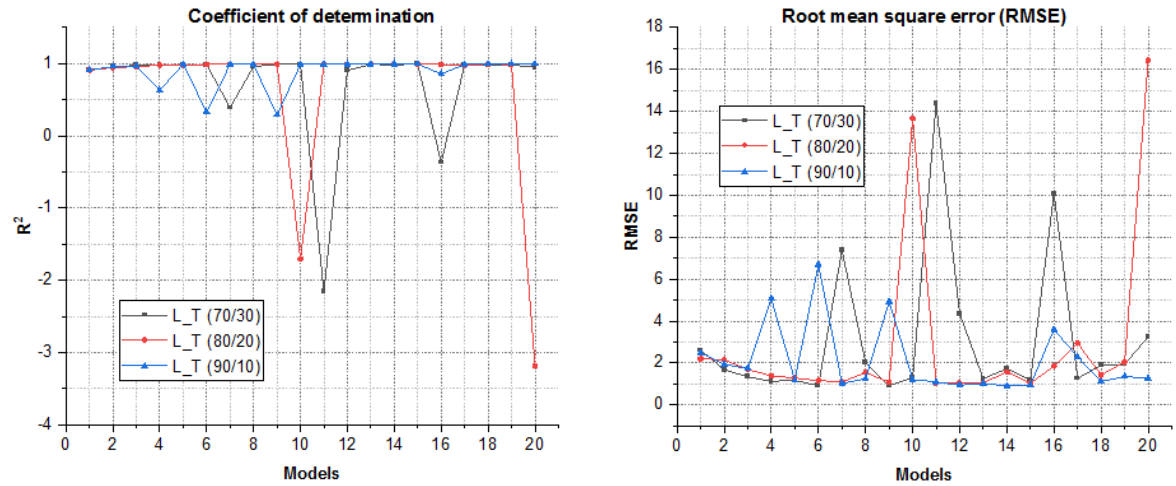

(c)

Fig. 13. Performance of 20 models evaluated by R2 and RMSE metrics as a function of activation; (a) logsig-purelin, (b) logsig-logsig and (c) logsig-tansig

This suggests an effective adaptation of the logsig activation function to the single hidden layer network with the backpropagation algorithm. Regarding Fig. 14, the RMSE values for training and testing also converge and start to decrease, except for some models exhibiting poor performance, likely due to improper learning.

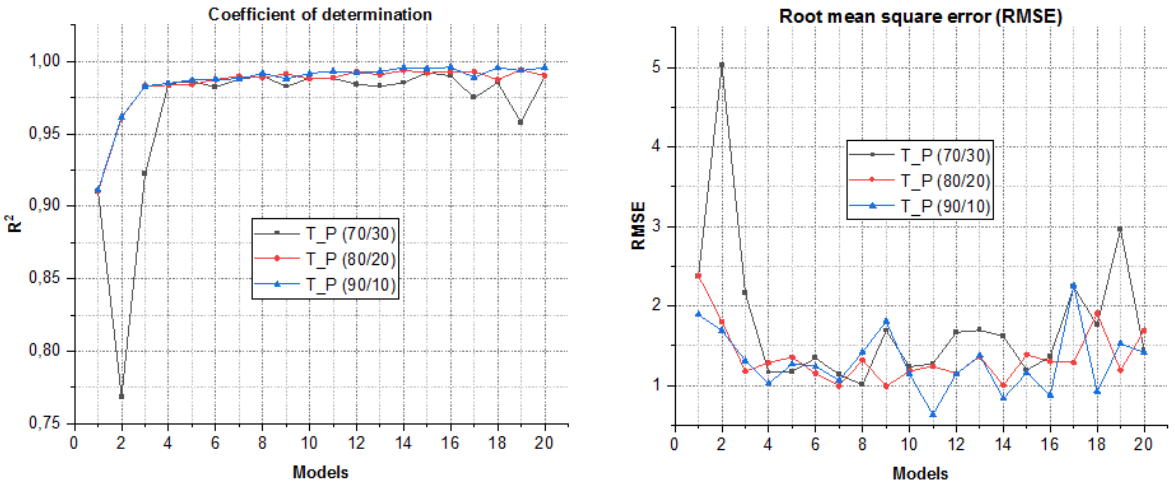

(a)

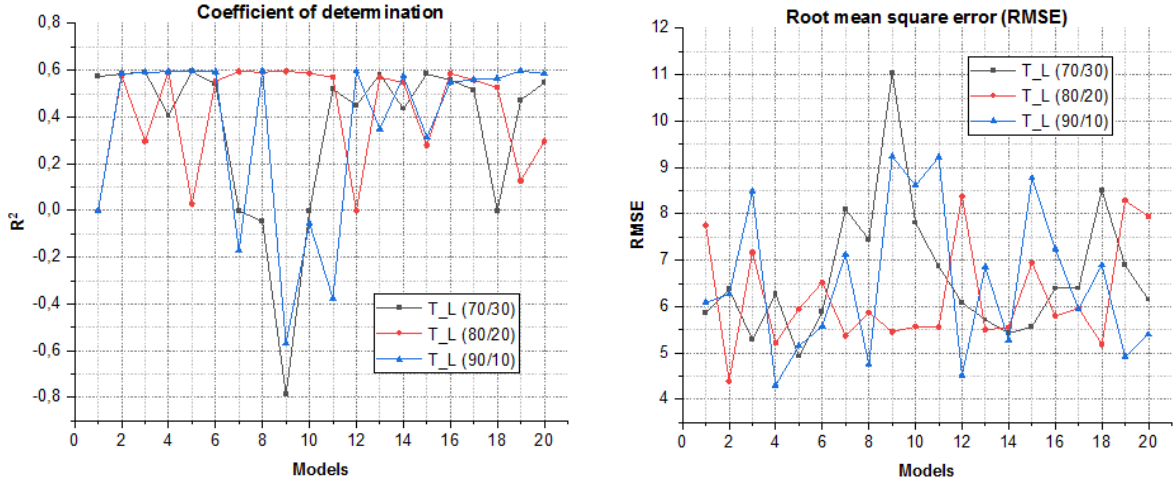

(b)

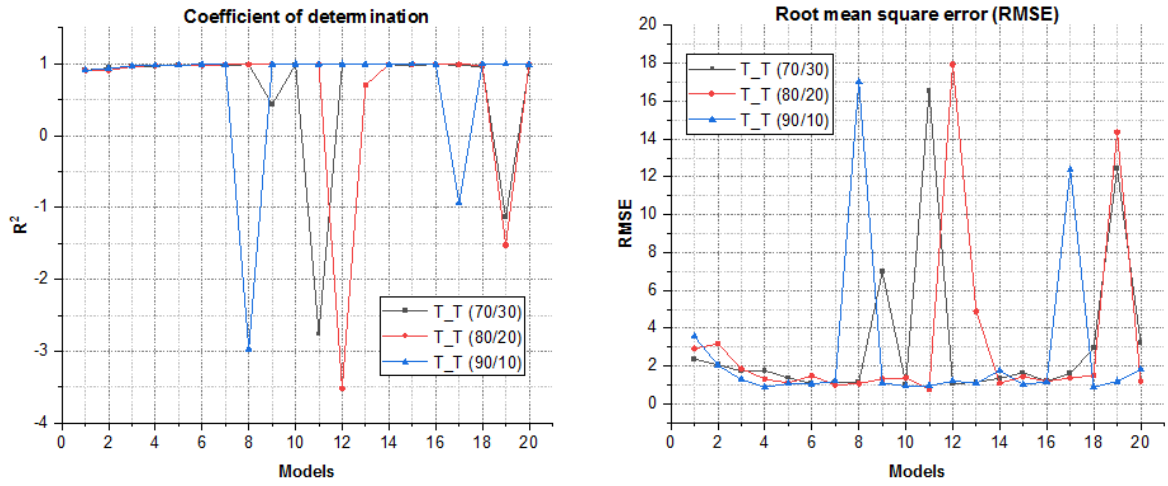

(c)

Fig. 14. Performance of 20 models evaluated by R2 and RMSE metrics as a function of activation;(a) tansig-purelin, (b) tansig-logsig and (c) tansig-tansig

The R^2 trends also begin to improve, especially in cases a and c, which approach the target, except for some samples that can be explained by an inadequate number of neurons for the activation functions and learning algorithm used.

The analysis of Figures 12, 13, and 14 demonstrates that the model providing the highest predictive accuracy, with minimal error, incorporates the *tansig* activation function in the hidden layer and *purelin* in the output layer. More specifically, Model 11 in case (a) of Fig.14. shows an RMSE value of 0.23 with a 90/10 data split (90% for training and 10% for testing). This result, among the lowest observed in all the models analyzed, testifies to an optimal performance thanks to this combination of activation functions. In addition, this RMSE value, remains lower than 1, indicating a high precision prediction on the entire dataset. This observation is reinforced by the metric of the coefficient of determination R^2, which reaches 0.992, thus approaching very close to 1. This value suggests that the model's predictions almost perfectly match the target values, indicating near-linear behavior. The overall analysis highlights the significant impact of activation functions and the data split ratio between training and testing on the neural network's performance, without requiring changes to other operational parameters.

To confirm the choice of model 11, we evaluated it using two additional metrics: the mean squared error (MSE) of testing and the correlation coefficient. Fig. 15. illustrates the training MSE, calculated by Matlab. This metric quantifies the arithmetic mean of the squares of the differences between the model predictions and the observed values. An MSE close to zero indicates that the model's predictions are very close to the actual values, reflecting high accuracy. The analysis of Fig. 15. reveals a training MSE of 0.467 over a total of 1000 epochs for the selected architecture. The MSE decreases rapidly as the artificial neural network (ANN) progresses in its learning. The two MSE curves coincide from the first epoch, suggesting an optimal match between the choice of activation functions, the data split ratio, and the backpropagation algorithm used. Consequently, this network is capable of providing accurate predictions regarding burst pressure.

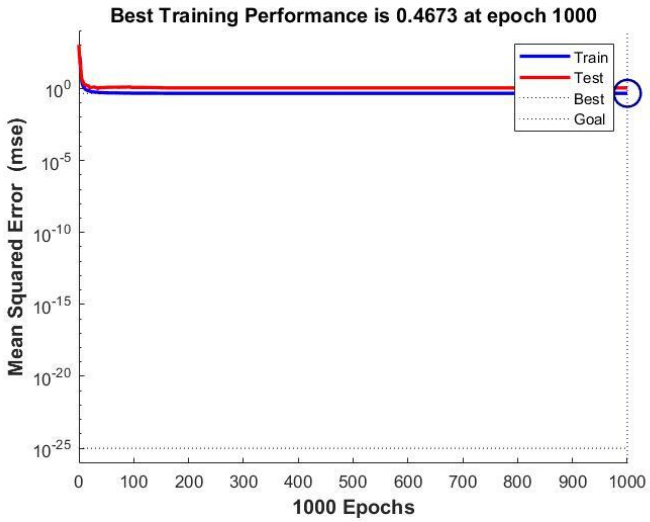

Fig. 15. MSE training

Fig. 16. generated using Matlab R2019a, provides details on the performance of the linear regression for the selected model. The correlation coefficient r measures the accuracy of predictions from a linear regression and ranges between 0 and 1. An r value close to 1 indicates an optimal fit of the model's predictions to the observed data, signifying an almost perfect correlation. Conversely, a value close to zero indicates a low correlation, suggesting that the model does not accurately reflect the data trends.

The correlation coefficient is crucial for forecasting future events using an established model, as it indicates how well past results can be used to predict future outcomes. According to the observations in Fig. 16. the r coefficient remains close to 1 throughout the evaluations, confirming the efficiency and relevance of the chosen model. This suggests not only that the model is well-

fitted but also that it is capable of providing reliable and accurate predictions, an essential aspect for any future deployment of the model in practical applications.

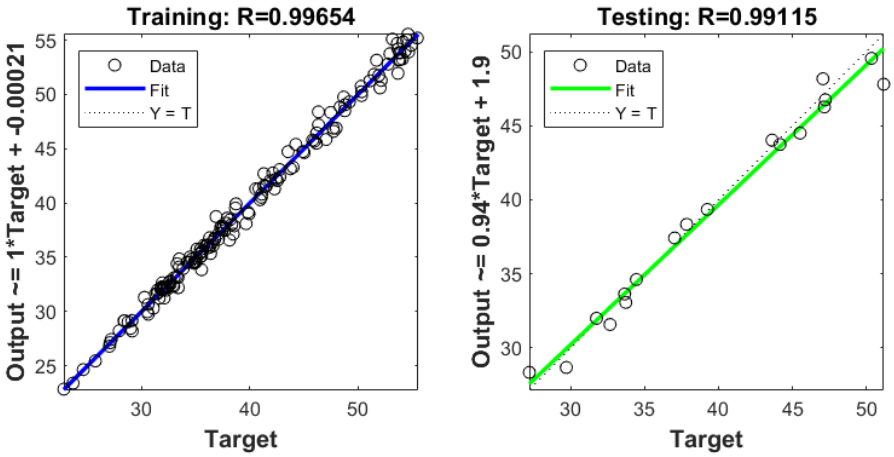

Fig. 16. Correlation coefficient

3. Results and Discussion

3.1. Topology of The Chosen Neural Network

In our study, we adopted a neural network model with a single hidden layer, as demonstrated in Fig. 17. The number of neurons in the input layer is equivalent to the number of variables in our dataset, which is 4, while the output layer consists of a single neuron representing the target variable of our dataset. The choice of 11 neurons for the hidden layer was justified by analyzing metrics such as RMSE, the coefficient of determination (R^2), the training MSE, and the correlation coefficient (r). This decision was made after multiple iterations exploring different configurations, from 1 to 20 neurons. Given the nature of our problem, which pertains to regression, we opted to use backpropagation trained with the Levenberg-Marquardt algorithm (ML) [53].

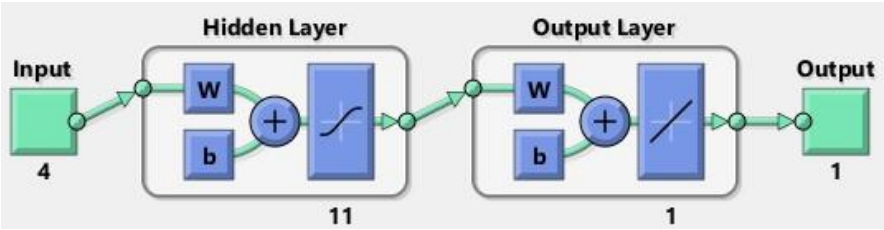

Fig. 17. The topology of the network under study

- Mathematical equation for the hidden layer

$$\begin{pmatrix} h_1 \\ h_2 \\ h_3 \\ h_4 \\ h_5 \\ h_6 \\ h_7 \\ h_8 \\ h_9 \\ h_{10} \\ h_{11} \end{pmatrix} = \begin{pmatrix} 0{,}241 & -1{,}230 & -0{,}583 & 1{,}765 \\ -8{,}605 & 0{,}540 & -8{,}864 & -1{,}954 \\ -6{,}304 & 0{,}887 & -0{,}109 & -0{,}046 \\ 0{,}461 & 2{,}649 & 1{,}789 & 4{,}073 \\ 16{,}749 & -0{,}271 & -0{,}091 & 1{,}292 \\ -0{,}078 & -0{,}461 & -3{,}111 & 0{,}907 \\ -40{,}564 & -25{,}244 & -81{,}911 & -24{,}195 \\ -0{,}087 & 0{,}043 & -3{,}177 & 0{,}406 \\ 1{,}272 & -1{,}067 & 0{,}165 & 1{,}624 \\ 0{,}142 & 17{,}184 & -0{,}504 & 18{,}631 \\ 2{,}047 & -0{,}359 & -0{,}737 & 0{,}232 \end{pmatrix} \begin{pmatrix} q \\ l \\ d \\ l/\sqrt{Dt} \end{pmatrix} + \begin{pmatrix} -0{,}619 \\ 12{,}752 \\ 6{,}104 \\ 3{,}442 \\ 8{,}111 \\ -1{,}437 \\ -35{,}484 \\ -1{,}468 \\ 1{,}097 \\ 3{,}818 \\ 1{,}240 \end{pmatrix} \quad (15)$$

- Equation for predicting burst pressure P_p using the selected neural network

$$P_p = f\left((1{,}503\ \ -0{,}109\ \ -0{,}967\ \ -0{,}083\ \ -0{,}891\ \ -11{,}433\ \ -0{,}030\ \ 11{,}106\ \ -1{,}215\ \ 0{,}057\ \ 0{,}579)\begin{pmatrix} f(h_1)\\ f(h_2)\\ f(h_3)\\ f(h_4)\\ f(h_5)\\ f(h_6)\\ f(h_7)\\ f(h_8)\\ f(h_9)\\ f(h_{10})\\ f(h_{11}) \end{pmatrix} + 1{,}423\right) \quad (16)$$

3.2. Differences Between FEA and ANN Burst Pressure Values

Fig. 18. compares burst pressure trends obtained from finite element analysis (P_n) with predictions from a neural network (P_p) for circumferential, parabolic, and rectangular defects. The close agreement between the curves generated by both methods, for each defect type, confirms the judicious selection of activation functions, network structure, and hidden layer neuron counts in the neural network model. The figure further permits the assessment of relative error between finite element simulation results and neural network predictions. This error is observed to be between 0% and 7% for circumferential defects, 0% and 4% for parabolic defects, and 0% and 5% for rectangular defects. These variations, although apparent, do not detract from the reliability of the model, as evidenced by consistently low error rates.

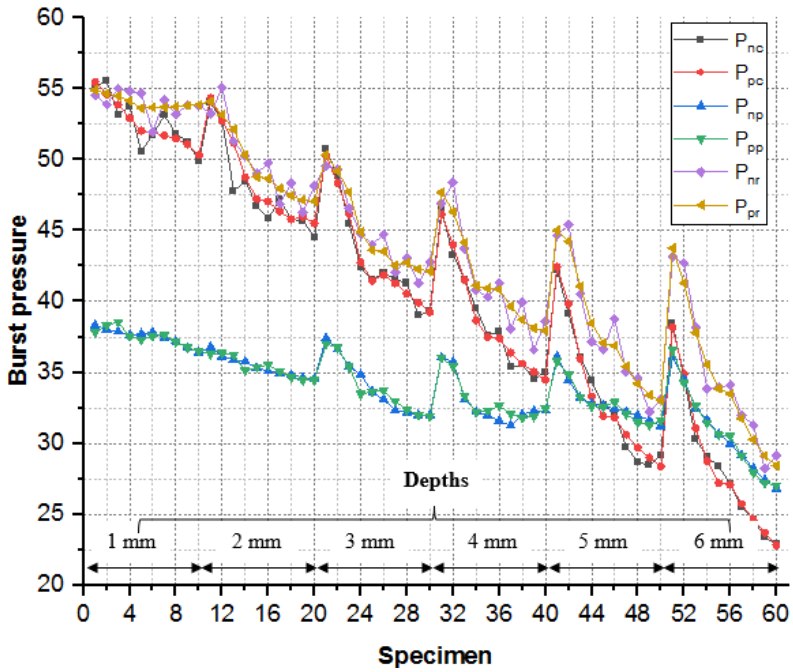

Fig. 18. Burst pressure evolution of simulation and neural network

Fig. 19. evaluates the performance of the neural network model against simulations, by presenting the distribution of relative errors (in %) for circumferential, parabolic, and rectangular defects, within a ±3σ range. The standard deviations observed for these defects are, respectively, 1.86, 1.19, and 2.23, indicating a low dispersion of errors. The entirety of the probability distributions lies within the ±3σ range, thus validating the selected neural network topology and its ability to meet the defined accuracy metrics. The application of the 3σ rule indicates that 99.73% of the errors are within the respective intervals of ±5.58%, ±3.57%, and ±6.69%, for the circumferential, parabolic, and rectangular defects. These reduced standard deviations confirm a low dispersion of errors, this robustness being attributable to the network topology and a judicious optimization of its parameters, as evidenced by the low maximal level of relative errors. These conclusions confirm that the adopted modeling method is appropriate for estimating burst pressure in the studied context.

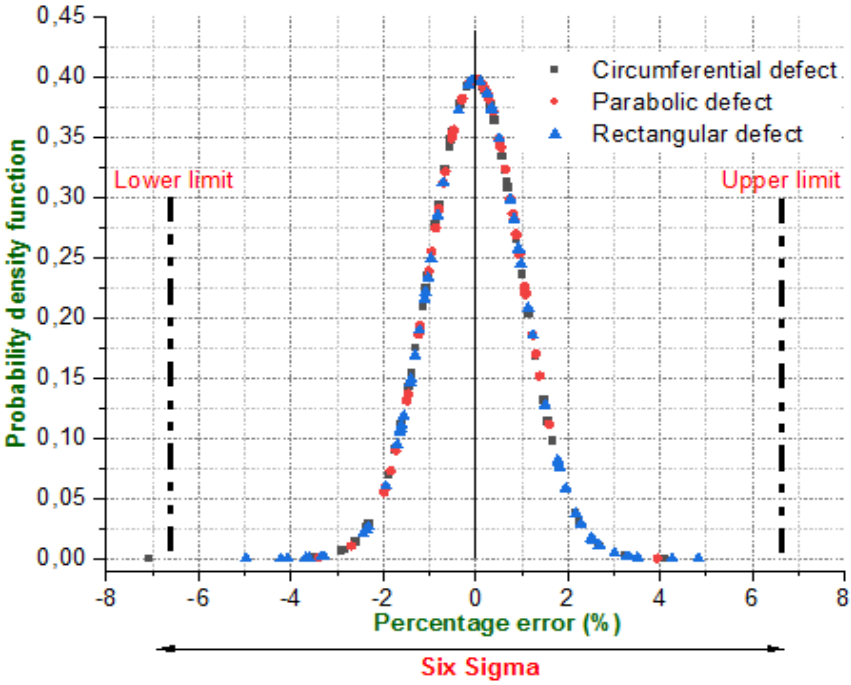

Fig. 19. Reduced normal distribution of the relative error between P_n and P_p

3.3. Discussion of the Harmfulness of The Three Corrosion Defects and Also the Geometrical Parameter Influencing Burst Pressure

Fig. 18. demonstrates a consistent decrease in burst pressure with increasing corrosion defect geometry across all three defect types. Initially, the burst pressure reduction is similar for rectangular and circumferential defects up to a depth of 4 mm; beyond this depth, the circumferential defect shows a more significant decrease, registering approximately 6 MPa lower. Given comparable defect dimensions, our results show that, generally, a parabolic defect remains more impactful than the other types. The figure also shows that at 5 mm depth and lengths of 120 and 220 mm, burst pressures for parabolic and circumferential defects become comparable. Furthermore, at 220 mm length and 5 mm depth, burst pressures for all three defects converge. Increasing defect depth, along with length, shows a progressive decrease in burst pressure, indicating a significant influence of defect depth on burst pressure. Cross-sectional analysis reveals that, with the exception of specific length ranges (160-220 mm at 5 mm depth and 80-220 mm at 6 mm depth) where the circumferential defect is most critical, the parabolic defect is consistently the most detrimental.

3.4. Recommendations and Limitations

The integration of artificial intelligence (AI) presents a paradigm shift from traditional, dataset-reliant methodologies, offering enhanced decision-making capabilities within the industrial sector. This study leverages AI to provide actionable insights for pipeline maintenance, specifically by accurately predicting burst pressures associated with rectangular, parabolic, and circumferential corrosion defects. Furthermore, the research proposes a prioritized intervention sequence for scenarios involving the simultaneous presence of these three distinct defect types across 2000 mm sections of pressurized pipelines. The developed neural network facilitates rapid burst pressure predictions, utilizing mathematical formulations (Eq (15) and (16)) within a mobile application, eliminating the need for computationally intensive finite element analysis in volumetric modeling software. However, this research acknowledges limitations regarding its broad applicability. Variations in pipeline materials and their associated Young's modulus may introduce inaccuracies in predictions. Moreover, the modeling of defects as ideal geometries necessitates expert interpretation when addressing real-world corrosion configurations.

4. Conclusions

This study investigates the impact of corrosion defects (parabolic, circumferential, longitudinal) on the rupture of pressurized pipelines, utilizing numerical simulations (SolidWorks validated by experimental data) to determine burst pressures.

Key Findings:

- Rectangular and circumferential defects exhibit a similar decrease in burst pressure up to a depth of 4 mm. Beyond this, the circumferential defect experiences a pressure drop approximately 6 MPa greater than the rectangular defect, warranting prioritized intervention.
- The parabolic defect is generally the most critical, except for certain length/depth combinations (160-220 mm at 5 mm, 80-220 mm at 6 mm) where the circumferential defect becomes the most detrimental.
- Similar burst pressures are observed for parabolic and circumferential defects at lengths of 120 mm and 220 mm (5 mm depth). At 220 mm/5 mm, all three defect types show nearly identical burst pressures.
- Burst pressure progressively decreases with increasing defect depth, with depth being the dominant parameter.

Neural Network Optimization:

The neural network topology was optimized through the analysis of metrics (RMSE, R^2, r, MSE) and by varying the training data distribution (70%, 80%, 90%) and test data distribution (30%, 20%, 10%) over 20 iterations. The final configuration, chosen for its optimal performance (RMSE and MSE < 1, R^2 and r ≈ 1), consists of 11 neurons in the hidden layer (hyperbolic tangent activation functions) and a linear output layer. This neural network accurately predicts burst pressures, as validated by the metrics, and advantageously replaces the computationally intensive Finite Element Analysis (FEA).

Future Directions:

This study aims to expand its scope by exploring other types of defects present in pressurized pipelines, analyzing their stress fields using advanced numerical simulations, and employing artificial intelligence techniques to formulate relevant recommendations for the industry. In the future, it would be beneficial to investigate the impact of stress corrosion cracking, which is a major factor in pipeline degradation. Furthermore, integrating real-time inspection data into the predictive model would enable the development of predictive maintenance systems capable of anticipating ruptures and optimizing interventions.

Nomenclature

DNV	DNV-RP-F101 corrosion assessment method	σ_u	Ultimate tensile strength
ANN	Artificial neural network	σ_{uts}	True ultimate tensile strength
FEA	Finite element analysis	E	Modulus of Elasticity
σ_c	Axial compressive stress	ϑ	Poisson's ratio
σ_y	Yield stress	D	Pipe outside diameter
σ_e	Effective von Mises stress	L	Length of pipe
σ_h	Hoop stress	t	Wall thickness
σ_r	Radial stress	d	Defect depth
σ_l	Axial/Longitudinal stress	l	Defect length
w	Defect width	r_i	Inside radius
3D	Three dimensional	MF	Folias factor
Q	Geometric correction factor	RMSE	Root Mean Squared Error
R^2	Coefficient of determination	r	Correlation coefficient
MSE	Mean squared error	q	Type of defects
P_p	Burst pressure via ANN	P_n	burst pressure via FEA

P_{tr}	Theorical burst pressure of rectangular defect	P_{tp}	Theorical burst pressure of parabolic defect
P_{tc}	Theorical burst pressure of circumferential defect	P_{nr}	Numerical burst pressure of rectangular defect
P_{pr}	Predicted burst pressure of rectangular defect	P_{np}	Numerical burst pressure of parabolic defect
P_{pp}	Predicted burst pressure of parabolic defect	P_{nc}	Numerical burst pressure of circumferential defect
P_{pc}	Predicted burst pressure of circumferential defect	Er,p	Relative error in the case of a parabolic defect
Er,c	Relative error for circumferential defects	h	Neuron output from hidden layer
Er,r	Relative error for rectangular defects	P_i	Failure pressure of intact pipe
n	Pre-activation	m	Number of samples
$\bar{y}$	Average targets value	$\hat{y}$	Predicted value
y	Target value		

References

[1] Zhang J, Liang Z, Han CJ. Effects of ellipsoidal corrosion defects on failure pressure of corroded pipelines based on finite element analysis. Int J Electrochem Sci. 2015;10(6):5036-47. https://doi.org/10.1016/S1452-3981(23)06684-1

[2] El Kiri Y, Mighouar Z, Zahiri L, Mansouri K, El Ouardi S, Chaiti H. Predicting the failure of plain dent pipeline subjected to cyclic loads using an artificial neural network. In: 2023 7th IEEE Congress on Information Science and Technology (CiSt); 2023; 179-86. https://doi.org/10.1109/CiSt56084.2023.10409983

[3] Li H, Huang K, Zeng Q, Sun C. Residual Strength Assessment and Residual Life Prediction of Corroded Pipelines: A Decade Review; 2022;15(3): 726. https://doi.org/10.3390/en15030726

[4] Mighouar Z, Khatib H, Zahiri L, Mansouri K. Comparison of the most harmful defects present in a steel pipe that can cause fatigue failure. IOP Conf Ser Mater Sci Eng. 2021;1126(1):012007. https://doi.org/10.1088/1757-899X/1126/1/012007

[5] Zakaria M, Zahiri L, Khatib H, Mansouri K. Effect of Water Hammer on Pipes Containing a Crack Defect; 2018.

[6] Zahiri L, Mighouar Z, Khatib H, Mansouri K, Salhi B. Fatigue Life Analysis of Dented Pipes Subjected to Internal Pressure.

[7] Zahiri L, El Houssine Ech-Chhibat M, Jammoukh M, Mighouar Z, Mansouri K. Numerical Modeling and Comparison of Defects Present in a Metal Pipe Under Internal Pressure. Solid State Technol. 2020;63(6):12821-32.

[8] Wang R, Kania R. IPC2016-64098; 2017. p. 1-7.

[9] Ireland GN, et al. Gas pipeline incidents 11; 2019.

[10] Fekete G, Varga L. The effect of the width to length ratios of corrosion defects on the burst pressures of transmission pipelines. Eng Fail Anal. 2012;21:21-30. https://doi.org/10.1016/j.engfailanal.2011.12.002

[11] Parvizsedghy L, Senouci A, Zayed T, Mirahadi SF, El-Abbasy MS. Condition-based maintenance decision support system for oil and gas pipelines. Struct Infrastruct Eng. 2015;11(10):1323-37. https://doi.org/10.1080/15732479.2014.964266

[12] Zakikhani K, Nasiri F, Zayed T. A review of failure prediction models for oil and gas pipelines. J Pipeline Syst Eng Pract. 2020;11(1):03119001. https://doi.org/10.1061/(ASCE)PS.1949-1204.0000407

[13] Razvarz S, Jafari R, Gegov A. A review on different pipeline defect detection techniques. In: Flow Modeling and Control of Pipeline Systems: A Formal Systems Approach; 2021; 25-57. https://doi.org/10.1007/978-3-030-59246-2_2

[14] Milošev I, Scully JR. Challenges for the Corrosion Science, Engineering, and Technology Community as a Consequence of Growing Demand and Consumption of Materials: A Sustainability Issue. Corrosion. 2023;79(9):988-96. https://doi.org/10.5006/4428

[15] Zahiri L, Khatib H, Ech-Chhibat ME. Fatigue-Corrosion Defect in a Metal Pipe Under Internal. 2020;

[16] Valor A, Caleyo F, Hallen JM. RISK16-8 744; 2016.

[17] American Society of Mechanical Engineers. Manual for Determining the Remaining Strength of Corroded Pipelines: A Supplement to ASME B31 Code for Pressure Piping: an American National Standard. American Society of Mechanical Engineers; 2012.
[18] Kiefner JF, Vieth PH. New method corrects criterion for evaluating corroded pipe. Oil Gas J. 1990;88(32).
[19] Wang LB. Development of Software for Residual Strength Evaluation and Residual Life Prediction of Corroded Pipelines. Xi'an Shiyou University, Xi'an, China; 2014.
[20] Stephens DR, Leis BN. Development of an alternative criterion for residual strength of corrosion defects in moderate-to high-toughness pipe. In: International Pipeline Conference; 2000. p. V002T06A012. https://doi.org/10.1115/IPC2000-192
[21] Det Norske Veritas. Corroded Pipelines. DNV; 2006.
[22] Lo M, Karuppanan S, Ovinis M. ANN-and FEA-based assessment equation for a corroded pipeline with a single corrosion defect. J Mar Sci Eng. 2022;10(4):476. https://doi.org/10.3390/jmse10040476
[23] Arumugam T, Karuppanan S, Ovinis M. Residual strength analysis of pipeline with circumferential groove corrosion subjected to internal pressure. Mater Today Proc. 2020;29(November 2018):88-93. https://doi.org/10.1016/j.matpr.2020.05.699
[24] Zahiri L, Khatib H, Ech-Chhibat ME. Fatigue-Corrosion Defect in a Metal Pipe Under Internal. 2020;8(10).
[25] Mighouar Z, Zahiri L, Khatib H, Mansouri K. Damage Accumulation Model for Cracked Pipes Subjected to Water Hammer. 2020;5(4):523-30. https://doi.org/10.25046/aj050462
[26] Cronin DS. Assessment of corrosion defects in pipelines. 2000.
[27] Su Y, Li J, Yu B, Zhao Y, Yao J. Fast and accurate prediction of failure pressure of oil and gas defective pipelines using the deep learning model. Reliab Eng Syst Saf. 2021;216(May). https://doi.org/10.1016/j.ress.2021.108016
[28] El Kiri YE, Zahiri L, Mansouri K, Mighouar Z. Prediction of the rupture pressure of a corroded pipeline by ANN. 2023;00031. https://doi.org/10.1051/e3sconf/202346900031
[29] Devi S, Kumar V, Karuppanan S, Ovinis M. An Empirical Equation for Failure Pressure Prediction of High Toughness Pipeline with Interacting Corrosion Defects Subjected to Combined Loadings Based on Artificial Neural Network. 2021.
[30] Kumar SDV, Karuppanan S, Ovinis M. Failure pressure prediction of high toughness pipeline with a single corrosion defect subjected to combined loadings using artificial neural network (ANN). Metals (Basel). 2021;11(2):373. https://doi.org/10.3390/met11020373
[31] Ren M, Zhang Y, Fan M, Xiao Z. Numerical Simulation and ANN Prediction of Crack Problems within Corrosion Defects. 2024. https://doi.org/10.3390/ma17133237
[32] Arumugam T, Karuppanan S, Ovinis M. Finite element analyses of corroded pipeline with single defect subjected to internal pressure and axial compressive stress. Mar Struct. 2020;72:102746. https://doi.org/10.1016/j.marstruc.2020.102746
[33] Xu W, Bao C, Choung J, Lee J. Corroded pipeline failure analysis using artificial neural network. Adv Eng Softw. 2017;0:1-12. https://doi.org/10.1016/j.advengsoft.2017.05.006
[34] Devi S, Kumar V, Karuppanan S, Ovinis M. Artificial Neural Network-Based Failure Pressure Prediction of API 5L X80 Pipeline with Circumferentially Aligned Interacting Corrosion Defects Subjected to Combined Loadings. 2022.
[35] Netto TA, Ferraz US, Estefen SF. The effect of corrosion defects on the burst pressure of pipelines. 2005;61:1185-204. https://doi.org/10.1016/j.jcsr.2005.02.010
[36] Chen Y, Wang W, Li X, Bai Y, Chen B, Li L. Ultimate load capacity of offshore pipeline with arbitrary shape corrosion defects. China Ocean Eng. 2015;29:241-52. https://doi.org/10.1007/s13344-015-0017-z
[37] Chen Z, Zhu W, Di Q, Wang W. Burst pressure analysis of pipes with geometric eccentricity and small thickness-to-diameter ratio. J Pet Sci Eng. 2015;127:452-8. https://doi.org/10.1016/j.petrol.2015.01.043
[38] Cronin DS, Pick RJ. Prediction of the failure pressure for complex corrosion defects. Int J Press Vessel Pip. 2002;79(4):279-87. https://doi.org/10.1016/S0308-0161(02)00020-0
[39] Wang YL, Li CM, Chang RR, Huang HR. State evaluation of a corroded pipeline. J Mar Eng Technol. 2016;15(2):88-96. https://doi.org/10.1080/20464177.2016.1224615
[40] Belachew CT, Che Ismail M, Karuppanan S. Strength assessment of corroded pipelines-Finite element simulations and parametric studies. Int J Struct Stab Dyn. 2017;17(07):1750069. https://doi.org/10.1142/S0219455417500699
[41] Baek J, Kim Y, Kim W, Koo J, Seok C. Load bearing capacity of API X65 pipe with dent defect under internal pressure and in-plane bending. Mater Sci Eng A. 2012;540:70-82. https://doi.org/10.1016/j.msea.2012.01.078
[42] Amaya-Gómez R, Sánchez-Silva M, Bastidas-Arteaga E, Schoefs F, Munoz F. Reliability assessments of corroded pipelines based on internal pressure-A review. Eng Fail Anal. 2019;98:190-214. https://doi.org/10.1016/j.engfailanal.2019.01.064

[43] Amandi KU, Diemuodeke EO, Briggs TA. Model for remaining strength estimation of a corroded pipeline with interacting defects for oil and gas operations. Cogent Eng. 2019;6(1):1663682. https://doi.org/10.1080/23311916.2019.1663682
[44] DNV CP. Recommended Practice DNV-RP-F101. Oslo, Norway: DNV; 2017.
[45] Batte AD, Fu B, Kirkwood MG, Vu D. New methods for determining the remaining strength of corroded pipelines. In: Proceedings of the international conference on offshore mechanics and arctic engineering; 1997. p. 221-8.
[46] Belachew CT, Ismail MC, Karuppanan S. Burst strength analysis of corroded pipelines by finite element method. J Appl Sci. 2011;11(10):1845-50. https://doi.org/10.3923/jas.2011.1845.1850
[47] Choi JB, Goo BK, Kim JC, Kim YJ, Kim WS. Development of limit load solutions for corroded gas pipelines. Int J Press Vessel Pip. 2003;80:121-8. https://doi.org/10.1016/S0308-0161(03)00005-X
[48] Wang YH, Wang GZ, Tu ST, Xuan FZ. In-plane and out-of-plane constraint characterization of different constraint parameters for semi-elliptical surface cracks in pipes. Eng Fract Mech. 2020;235:107161. https://doi.org/10.1016/j.engfracmech.2020.107161
[49] Bai B, Zhang J, Wu X, Zhu GW, Li X. Reliability prediction-based improved dynamic weight particle swarm optimization and back propagation neural network in engineering systems. Expert Syst Appl. 2021;177:114952. https://doi.org/10.1016/j.eswa.2021.114952
[50] Laabid Z, Moumen A, Mansouri K, Siadat A. Numerical study of the speed's response of the various intelligent models using the tansig, logsig and purelin activation functions in different layers of artificial neural network. IAES Int J Artif Intell. 2023;12(1):155. https://doi.org/10.11591/ijai.v12.i1.pp155-161
[51] Chicco D, Warrens MJ, Jurman G. The coefficient of determination R-squared is more informative than SMAPE, MAE, MAPE, MSE and RMSE in regression analysis evaluation. PeerJ Comput Sci. 2021;7:e623. https://doi.org/10.7717/peerj-cs.623
[52] Rodríguez Sánchez A, Salmerón Gómez R, García C. The coefficient of determination in the ridge regression. Commun Stat Comput. 2022;51(1):201-19. https://doi.org/10.1080/03610918.2019.1649421
[53] Sapna S, Tamilarasi A, Kumar MP. Backpropagation learning algorithm based on Levenberg Marquardt Algorithm. Comput Sci Inf Technol (CSIT). 2012;2:393-8. https://doi.org/10.5121/csit.2012.2438